Eco-Friendly and Solar light Active Ti-Fe2O3 Ellipsoidal Capsules Nanostructure for Removal of Herbicides and Organic Dyes

Hanan Mohamed (m_h_hanan_0503@yahoo.com)
Helwan University Faculty of Science
Dina H. Besisa
CMRDI: Central Metallurgical Research and Development Institute

Research Article

Keywords: Green Ti-Fe2O3, ellipsoidal capsules, solar photocatalysis, BPB dye, 2,4-D

Posted Date: March 24th, 2022

DOI: https://doi.org/10.21203/rs.3.rs-1421603/v1

Abstract

In this work, Ti doped Fe_2O_3 with hollow ellipsoidal capsules nanostructure has been prepared in a green manner using plant extract (Flax seed). This new green hematite nanomaterial has been evaluated as photocatalyst for water treatment by testing its activity for degradation of bromophenol blue dye (BPB) and 2,4-dichlorophenoxy acetic acid (2,4-D) herbicide. For a better understanding of the green material properties, a comparison with the pristine Fe_2O_3 nanospheres previously prepared by the same procedure is included. Structural and optical properties of the green prepared materials are studied. The results revealed the success doping of Ti^{4+} at Fe^{3+} site, without forming any of TiO_2 phases. It was also found that, the Ti doping is resulted in the reduction of the band gap of Fe_2O_3 as well as changing the morphology. The Ti-doped Fe_2O_3 nanomaterial exhibited an enhanced photocatalytic activity either for BPB dye or for 2,4-D degradation with more than 2 times higher rate than that using pristine Fe_2O_3.

1. Introduction

The world is facing a critical shortage of clean water supplies as resulted from global population growth and industrialization. So that, most of our water resources including surface and ground water are so polluted and dangerous that it can't even be used for industrial purposes. Dyes exist in water from textile, leather, and tuning industries represent a growing environmental concern (Sharma et al. 2017; Liu 2020). Dye molecules possess aromatic rings in their structure, which render them with a high biodegradation resistance, high toxicity and carcinogenic. In addition, they prevent the penetration of solar light and delay the photosynthetic reaction which significantly affecting the aquatic life (Lellis et al. 2019). Moreover, about 80% of pesticides and herbicides are directly leached into groundwater causing major environmental issue. Besides being carcinogenic, pesticides and herbicides are regarded as endocrine disrupting chemicals, causing adverse effects on the endocrine system, reproductive system and immunologic system of human and animals (Syafrudin et al. 2021). Photocatalysis using semiconductor nanomaterials and solar energy, is considered as the most promising solution to address the challenges concerning water purification form such organic pollutants and other inorganic and biological pollutants (Ren et al. 2021). However, the photocatalytic efficiency of semiconductor nanomaterials is still limited by low activity and limited solar light harvesting that makes the photocatalytic system not applicable in real [6]. Tremendous efforts have been devoted to address this issue tailoring photocatalytic nanomaterials with different types and microstructures (Thongam and Chaturvedi 2021).

Among metal oxide semiconductors, hematite (Fe_2O_3) has drawn scientific interest due to its outstanding properties such as chemical and thermodynamical stability, high solar light absorptivity (absorbs ~ 40% of visible light) and non-toxicity (Asif et al. 2021; Mishra and Chun 2015). Various physical and chemical methods have been reported on the synthesis of hematite nanomaterials such as co-precipitation (Fouad and Zhang 2019), thermal decomposition (Samrot et al. 2021), sol–gel (Samrot et al. 2021) and hydrothermal method (Tadic et al. 2019). Nowadays, green synthetic methods using plant extract have drown special scientific interests as being clean, cheap, simple and safe, in addition to their enhancement

of the nanoparticle's morphology (Mohamed et al. 2019; Al-Hakkani et al. 2021; Rostamizadeh et al. 2020).

Despite the characteristic properties of Fe_2O_3, its small band gap (1.9–2.2 eV) reducing its catalytic performance due to low conductivity and rapid recombination of charge carriers (Li and Chu 2018). Several attempts were applied to overcome this problem such as doping (Yina et al 2018), modifying nanostructure (Chen and Lin 2017) or coupling with other semiconductor (Bora 2016). An effective process is doping with other transition metal ions, such as Zn^{2+}(Suman et al. 2020), Ni^{2+} (Liu et al. 2012), Co^{2+} (Keerthana et al 2021), Al^{3+} (Kleiman-Shwarsctein et al. 2010), Sn^{4+} (Popov et al. 2022; Em et al. 2022), and Ti^{4+} (Fu et al 2014; Biswas et al. 2020). Generally, during doping, the orbital hybridization takes place between the dopant orbital and molecular orbital of host, which leads to a tunable electronic structure and controllable potentials of the VB and the CB. Doping by transition metal ions leads to the generation of new energy levels within the bandgap area (donor level above the VB or acceptor level below the CB) of the photocatalyst. This results in sub-band-gap irradiation from which the electrons have the ability to be excited from the d-band of the dopant to the CB of the host photocatalyst or from the VB of the host photocatalyst to the d-band of the dopant by photons with lower energy than that required by the un-doped photocatalyst (Shao et al. 2018). Moreover, the importance of transition metal doping is represented by the formation of the trapping levels and their ability to tune some properties of the semiconductors such as electrical, optical and therefore photocatalytic properties. For instance, the non isovalent substitution of Zn^{2+} at Fe^{3+} site resulted in charge imbalance in Fe_2O_3 lattice. Three mechanisms have been proposed to preserve the neutrality of charges, includes $Fe^{3+} \rightarrow Fe^{2+}$ transformation, creation of cation vacancies and filling of oxygen vacancies (Suman et al. 2020). In addition, doping with tetravalent metal ion, which can form a covalent bond with the oxygen leads to increase the number of charge carriers, hence increasing the conductivity. For example, doping of with Sn^{4+} ions have greatly improved gas sensing and photoelectrochemical properties of Fe_2O_3 nanoparticles and thin films (Popov et al. 2022). Similarly, Ti-doped Fe_2O_3 can greatly enhance the electron-hole pair separation as well as increase the charge density, therefore improves the photocatalytic and photoelectrochemical activity (Fu et al 2014; Biswas et al. 2020). It was hypothesized that; the enhanced performance of Ti-treated hematite is due to the formation of Fe_2TiO_5-instead of substitution of Fe in Fe_2O_3 by Ti (Deng et al. 2015).

Several studies have been reported on producing Ti-treated (or doped) hematite nanostructure arrays for solar water splitting and electrochemical applications (Fu et al 2014; Biswas et al. 2020; Deng et al. 2015). However, none of them studied green production of Ti doped hematite nanostructures or using the produced Ti-treated Fe_2O_3 nanomaterials for photocatalytic degradation of organic pollutants. Based on this, we have eco-friendly synthesized Ti-doped Fe_2O_3 nanostructure, using plant extract, and studied their structural, optical, and morphological properties in comparison with pristine Fe_2O_3. Furthermore, the effect of Ti doping on the photocatalytic degradation of organic pollutants has been investigated in this study.

2. Experimental

2.1. Materials Synthesis

Flax seed extract was prepared according to previous work (Mohamed et al. 2019). Typically, a specific amount of washed and grinded FS powder was dissolved in distilled water then heated until boiling. The resulted suspension of FS extract was filtered and then stored in the fridge for further use.

Ti-Fe_2O_3 nanoparticles were synthesized from $Fe(NO_3)_3.9H_2O$ as α-Fe_2O_3 precursor and TTIP ($Ti\{OCH(CH_3)_2\}_4$) as Ti source. Typically, FSE suspension is drop-wise added to an aqueous Fe^{3+} solution under ultrasonic vibration for 2 hrs at 50 ºC. After that, 5% of TTIP is dropwise added to the above suspension and left stirring for 30 min. The final solid products were separated from the formed suspension by centrifugation, washed two times by distilled water using centrifugation and then dried at 70°C for 1h. Pure Fe_2O_3 was prepared by the same method without adding TTIP.

2.2. Characterization

XRD measurements were performed using a Cu-K x-ray with tube conditions of 40 kV. SEM images were taken by using FEI, Inspect S50 at accelerating voltage of 20 kV. TEM analysis was performed on TEM FEI, Morgagni 268, Brno, Czech Republic. DRS measurements were recorded on Jasco V760 spectrometer and UV–vis absorption measurements were recorded on UVD-3200, LABOMED.

2.3. Photocatalytic Activity

The photocatalytic activity of hematite nanomaterials was evaluated for the degradation Bromophenol Blue (BPB) dye as model dye and 2,4-Dichlorophenoxyacetic acid (2,4-D) as model herbicide. In a typical photocatalytic experiment, 1 g/l of the photocatalyst was ultrasonically dispersed in pure water. Then 20 mg/L aqueous solution of the water pollutant (BPB dye or 2,4-D) was added to the catalyst's suspension. Prior to the photoirradiation, the adsorption of the organic molecules on the surface of the photocatalyst was tested by stirring the photocatalyst/ organic pollutants (BPB or 2,4-D) suspension in the dark for 30 min. After that the photo-irradiation was carried out at room temperature using a solar lamp (30 W) under stirring. To determine the change in the concentration of the organic pollutant with time, liquid samples of the photocatalyst/pollutant suspension were taken, filtered from the photocatalyst particles and then measured by the UV-vis spectrophotometer.

The photocatalytic degradation efficiency has been determined using the following equation:

$$\text{Photodegradation Efficiency \%} = \frac{C_0 - C_t}{C_0} \times 100 = \frac{A_0 - A_t}{A_0} \times 100$$

where C_0 is the initial concentration of pollutant and C_t is the pollutant's concentration at certain reaction time t (min). The kinetics of the photocatalytic experiments has been determined by plotting $-ln\frac{C_t}{C_0}$

versus time which should yield straight lines slope of the apparent first order rate constant *k* according to the following equation:

$$-ln\frac{C_t}{C_0} = kt$$

3. Results And Discussion

3.1. Materials Characterization

Characterization of FSE

UV–vis DRS of FSE, shows a broad absorption in the visible region which is attributed to the presence of antioxidants in the FSE (see Figure S1(a)). FTIR spectroscopic measurement of FSE (Figure S1(b)) confirms the presence of polyphenolic and phenolic compounds as indicated from the band at ~ 3400 cm^{-1} for -OH stretching vibration (Butsat et al. 2010). The GC–MS measurement confirms the existence of carbohydrate, esters, and cyclononasiloxane compounds in addition to polyphenolic compounds (Figure S1(c)) (Mohamed et al. 2019). Based on this, the compounds in the aqueous extract of FS are supposed to act as inducing and stabilizing agent during the formation of the nanomaterials. The mechanism of preparation of Ti-Fe_2O_3 nanomaterial using FSE can be described by the following equation:

$$2Fe^{3+} + 4OH - [FSE] \xrightarrow{Ultrasound,\ 50^\circ C} 2FeOOH + 2H^+ \quad \textit{(Eq. 1)}$$

$$2FeOOH + Ti^{4+} \xrightarrow{500^\circ C} Ti - Fe_2O_3 + H_2O \quad \textit{(Eq. 2)}$$

Characterization of Nanomaterials

The XRD patterns of hematite nanomaterials are shown in Fig. 1. The diffraction peaks of both pure Fe_2O_3 and Ti-Fe_2O_3 are well indexed to rhombohedral hematite at 24.13º, 33.15º, 35.612º, 40.85º, 49.48º, 54.09º, 57.59º, 62.41º and 63.99º. The XRD results revealed the formation of pure and well crystalline α-Fe_2O_3, which are in good agreement with the previous reports (Mohamed et al. 2019; Rahman et al. 2013). The identical XRD patterns of pure- and Ti doped Fe_2O_3 indicating that Ti^{4+} ions have substituted, at least partially, Fe^{3+} ions in the hematite matrix without changing the rhombohedral structure. Moreover, the intensity of the peaks is higher for Ti-Fe_2O_3, and its half height width is also higher than pure hematite. The results revealed the increase of the grain size of the Ti doped hematite. In addition, small shift to a larger diffraction angle is obvious for the diffraction peaks of Ti-Fe_2O_3 (see inset of Fig. 1). This shift has been correlated to the substitution of the smaller Ti^{4+} ions (ionic radius = 0.061 nm) into the larger Fe^{3+} ions (ionic radius = 0.069 nm) of Fe_2O_3 (Hwang and Jung 2022) (Inset of Fig. 1).

The morphological features of the pure and Ti doped Fe_2O_3 were investigated by SEM and TEM. SEM image (Fig. 2) shows the homogeneous spherical shaped particles of α-Fe_2O_3, while the SEM image of Ti-Fe_2O_3 shows homogeneous open hollow ellipsoidal capsules structure. TEM images of pure and Ti-doped Fe_2O_3 nanostructures are shown in Fig. 3. Nanospheres of pure Fe_2O_3 have diameter range of 100–300 nm, while ellipsoidal capsules of Ti-doped Fe_2O_3 have width range of 400–500 nm and length range of 600–800 nm. The change in the morphology of hematite upon Ti doping can be attributed to the synthesis procedure applied in this work since the in-situ methods usually alter the crystalline structure and morphology of the doped material, in addition to the effect of the dopant precursor during nanoparticle growth (Kusior et al. 2019).

The FTIR spectra of pure and Ti-Fe_2O_3 nanostructures show two main peaks at 467–476 cm^{-1} assigned to bending vibration of O–Fe–O and at 555–557 cm^{-1} referred to the stretching vibrations of Fe–O bonds (Mohamed et al. 2019; Rahman et al. 2013; Zielinska et al. 2010). The peaks at 1625 and ~ 3420 cm^{-1} are corresponding to the –OH stretching vibrations (Fig. 4) (Mohamed et al. 2019; Rahman et al. 2013; Zielinska et al. 2010). By a comparison with pure Fe_2O_3, the broad peak at 3420 cm^{-1} is suppressed for Ti-Fe_2O_3 which may be due to a lower hydroxylation level due to Ti doping. It is concluded that the non-isovalent substitution of Ti^{4+} at Fe^{3+} sites can induce structural modifications of the hematite surface, preventing from reaching the full hydroxylation.

UV-vis Diffuse Reflectance measurements (Fig. 5 (a)), show high absorption in the visible region with absorption edge of ~ 580 nm for pure Fe_2O_3. The absorption edge is shifted to ~ 610 nm for Ti-Fe_2O_3. The band gap energy of the samples has been estimated from the intercept of the tangents of Kubelka-Munk plots to be 2.13 and 2.03, for pure Fe_2O_3 and Ti-Fe_2O_3 respectively (Fig. 5 (b)). The shift of the band gap energy of Ti doped Fe_2O_3 to lower energy can be attributed to the increase in structural disorder or defects with Ti doping. This decrease in the band gap of Ti-Fe_2O_3 compared with the Fe_2O_3 could be also attributed to the introduction of additional energy level below the conduction band of Fe_2O_3 by Ti doping.

3.2. Photocatalytic Activity

Photocatalytic degradation of BPB

Figure 6 (a) shows the absorption spectra for degradation of BPB dye solution in the presence of Ti-Fe_2O_3 under solar light irradiation. The UV-vis absorption spectrum of BPB shows a maximum absorbance at 590 nm and another small peak at 380 nm. The absorption peak at 590 nm decreased rapidly with irradiation time. After 2 h of light irradiation, about 95% of the dye has been degraded. For comparison, BPB degradation has been evaluated using pure Fe_2O_3 at the same experimental conditions. The degradation efficiency of both nanomaterials are shown in Fig. 6 (b). The pseudo-first order kinetics of the absorption data is shown in Fig. 6 (c). The observed rate constant (k_{obs}) is estimated as 0.012 and 0.026 min^{-1} for pure Fe_2O_3 and Ti-Fe_2O_3, respectively, indicating that, the photocatalytic activity of the Ti-

Fe_2O_3 is more than 2 folds higher than that of pure Fe_2O_3 nanomaterial. The results can be explained by the improvement of conductivity and photoactivity of hematite due to the non-isovalent substitutional doping by introducing Ti^{4+} into hematite. Though there is an argument on explaining the improvement of photoactivity of Ti-Fe_2O_3 on whether the effect of Ti^{4+} ions as donor, or due to the small polaron hopping ($Fe^{3+}+Ti^{4+}\rightarrow Fe^{2+}+Ti^{3+}$), it has not been proved in our study.

The recyclability of Ti-Fe_2O_3 was tested for 3 runs used in degradation of BPB (Fig. 6 (d)). No noticed decrease in the activity of the photocatalyst observed revealing the high stability of the Ti-Fe_2O_3 nanomaterial.

Photocatalytic degradation of 2,4-D

The photocatalytic degradation of 2,4-D, an organic pollutant frequently exists as the agricultural effluent, was also evaluated using hematite nanomaterials. Figure 7 (a) shows the UV-vis absorption spectra for the degradation of 2,4-D under solar light irradiation in the presence of Ti-Fe_2O_3. The UV–vis spectrum of 2,4-D shows 2 main peaks at 285 and 230 nm. The peak at 285 nm is specified to the $n\rightarrow\pi^*$ transitions of the C–Cl bonds and the peak at 230 nm is assigned to $\pi\rightarrow\pi^*$ transition of aromatics rings (González et al. 2020). After 30 min in the dark ~ 6% of the herbicide molecules have been adsorbed on the surface of Ti-Fe_2O_3. After solar light irradiation, the characteristic peak at 230 nm was found to be decreased rapidly with irradiation time, while, from 30 to 90 min irradiation, a significant increase in absorbance is observed in the region 240–270 nm which can be attributed to the formation of benzoquinones intermediates [35]. Moreover, higher decrease in the intensity is observed for the peak at 230 nm as compared to the peak at 285 nm, indicating that the C = C bonds in the aromatic ring of 2,4-D molecule are more likely to be degraded by •OH than the C-Cl bond. After ~ 4 h, almost all 2,4-D has been degraded. Thus, 2,4-D is mainly degraded by electrophilic attack of hydroxyl radical to aromatic compounds and C-Cl bands, to produce primary organic acid such as acetic and formic acid (Ng et al. 2010), which are finally mineralized to CO_2 and H_2O. The degradation kinetics of 2,4-D has been evaluated by monitoring the change in the absorption at 230 nm (Fig. 7 (b)). The pseudo-first order kinetics of the absorption data is shown in Fig. 7 (c) with k_{obs} 0.0048 min^{-1} and 0.0109 min^{-1}, for pure Fe_2O_3 and Ti-Fe_2O_3, respectively. It is obvious that, the photocatalytic degradation efficiency of the herbicide compound is more than two times higher using Ti-Fe_2O_3 as compared to pure Fe_2O_3 nanomaterial. The kinetic data are summarized in Table 1. This enhancement in the photocatalytic activity can be readily explained by the enhancement of the photogenerated charge separation upon Ti doping. It has been also reported that the photogenerated holes can be captured and stored at Ti^{4+} sites on the surface of Fe_2O_3, facilitating their transfer to the surface reactant (Liu et al. 2017). In addition, the higher photocatalytic activity can be attributed to the synergistic effect of the high specific area of the open hollow ellipsoidal capsule's structure of Ti-Fe_2O_3 and the enhanced charge separation, upon Ti doping.

Table 1
Kinetic parameters for the degradation of BPB and 2,4-D using hematite nanomaterials

Nanomaterial	Reactant	k (min^{-1})	R^2
Fe_2O_3	BPB	0.012	0.99
Ti/Fe_2O_3	BPB	0.026	0.99
Fe_2O_3	2,4-D	0.0048	0.99
Ti/Fe_2O_3	2,4-D	0.0109	0.98

4. Conclusions

In summary, pristine and Ti doped Fe_2O_3 has been successfully prepared in green manner using FS extract. Structural, Optical, and morphological properties of the green hematite nanomaterials have studied by XRD, FTIR, SEM, TEM and DRS. XRD and FTIR confirmed the success doping of Ti^{4+} at Fe^{3+} site of hematite without forming new phases (e.g., TiO_2). SEM and TEM showed the change in the morphology of the hematite upon Ti doping, which was attributed to the effect of the in-situe doping method as well as the effect of the dopant precusor. DRS results showed an increase in the absorption edge for the Ti-Fe_2O_3, and the Kubellka-Munk estimated band gap energy was found to be reduced to be 2.03 eV as compared to pristine Fe_2O_3 (2.13 eV). This reduction in the band gap was attributed to the increase in structural disorder or defects with Ti doping as well as to the introducing of additional energy level below the conduction band of Fe_2O_3 upon Ti doping. Furthermore, the photocatalytic activity of undoped and Ti doped hematite nanomaterials was studied for the degradation of BPB dye and 2,4-D herbicides as model water pollutants. The photocatalytic degradation efficiency of BPB dye as well as herbicide compound was found to be more than two times higher using Ti-Fe_2O_3 as compared to pure Fe_2O_3 nanomaterial. This enhancement of the activity was readily due to the enhancement of e^-/h^+ pair separation, as well as to the synergistic effect of the high area of the open hollow ellipsoidal capsule's structure of Ti-Fe_2O_3 and the increased donor density.

Declarations

Acknowledgements

Dr. Hanan H. Mohamed is gratefully acknowledged Faculty of Science. Helwan University for providing facilities.

Declaration of interests

The authors declare that they have no known competing financial interests or personal relationships that could have appeared to influence the work reported in this paper.

Ethical Approval

Not Applicable.

Consent to Participate

Not Applicable.

Consent to Publish

Not Applicable.

Authors Contributions

All authors contributed to the study conception, design, material preparation, data collection and analysis. The first draft of the manuscript was written by Hanan H. Mohamed and all authors commented on previous versions of the manuscript. All authors read and approved the final manuscript.

Funding

The authors declare that no funds, grants, or other support were received during the preparation of this manuscript

Availability of data and materials

Not Applicable.

References

1. Al-Hakkani MF, Gouda GA, Hassan SHA (2021) A review of green methods for phyto-fabrication of hematite (α-Fe_2O_3) nanoparticles and their characterization, properties, and applications. Heliyon 7:e05806
2. Asif AH, Wang S, Sun H (2021) Hematite-based nanomaterials for photocatalytic degradation of pharmaceuticals and personal care products (PPCPs): A short review. Curr Opin Green Sustainable Chem 28:100447
3. Biswas P, Ainabayev A, Zhussupbekova A et al (2020) Tuning of oxygen vacancy-induced electrical conductivity in Ti-doped hematite films and its impact on photoelectrochemical water splitting. Sci Rep 10:7463
4. Bora D (2016) The photocathodic behavior of hierarchical ZnO/hematite hetero nanoarchitectures. J Mater Res 31:1554–1564

5. Butsat S, Siriamornpun S (2010) Antioxidant capacities and phenolic compounds of the husk, bran and endosperm of Thai rice. Food Chem 119:606–613
6. Chen YH, Lin CC (2014) Effect of nano-hematite morphology on photocatalytic activity. Phys Chem Minerals 41:727–736
7. Deng J, Lv X, Liu J, Zhang H, Nie K et al (2015) Thin-Layer Fe_2TiO_5 on Hematite for Efficient Solar Water Oxidation. ACS Nano 9:5348–5356
8. Em S, Yedigenov M, Khamkhash L, Molkenova A, Atabaev TSh (2022) Sn-Doped Hematite Nanoparticles for Potential Photocatalytic Dye Degradation. J Phys Chem Solids 161:110372
9. Fouad DE, Zhang C, El-Didamony H, Yingnan L, Mekuria TD, Shah AH (2019) Improved size, morphology and crystallinity of hematite (α-Fe_2O_3) nanoparticles synthesized via the precipitation route using ferric sulfate precursor. Results in Physics 12:1253–1261
10. Fu Z, Jiang T, Liu Z, Wang D, Wang L, Xie T (2014) Highly photoactive Ti-doped α-Fe_2O_3 nanorod arrays photoanode prepared by a hydrothermal method for photoelectrochemical water splitting. Electrochim Acta 129:358–363
11. González AE, Asomoza M, Solís S, Sánchez MAG (2020) Cipagauta-Díaz S Enhanced photocatalytic degradation of the herbicide 2,4-dichlorophenoxyacetic acid by Pt/TiO_2–SiO_2 nanocomposites. Reaction Kinetics Mechanisms and Catalysis 131:489–503
12. Hwang JS, Jung KY (2022) Effect of calcination temperature and Ti substitution on optical properties of (Fe,Cr) O cool black pigment prepared by spray pyrolysis. RSC Adv 12:72–77
13. Keerthana SP, Yuvakkumar R, Ravi G, Kumar P, Soliman Elshikh M, Alkhamis HH, Alrefaei AF, Velauthapillai D (2021) A strategy to enhance the photocatalytic efficiency of α-Fe_2O_3. Chemosphere 270:129498
14. Kleiman-Shwarsctein A, Huda MN, Walsh A, Yan Y, Stucky GD, Hu YS, Al-Jassim MM, McFarland EW (2010) Electrodeposited Aluminum-Doped α-Fe_2O_3 Photoelectrodes: Experiment and Theory. Chem Mater 22:510–517
15. Kusior A, Michalec K, Jelen P, Radecka M (2019) Shaped Fe_2O_3 nanoparticles – Synthesis and enhanced photocatalytic degradation towards RhB. Appl Surf Sci 476:342–352
16. Lellis B, Fávaro-Polonio CZ, Pamphile JA, Polonio (2019) Effects of textile dyes on health and the environment and bioremediation potential of living organisms. Biotechnol Res Innov 3:275–290
17. Li J, Chu D (2018) 4-Energy band engineering of metal oxide for enhanced visible light absorption, Editor(s): Zhiqun Lin, Meidan Ye, Mengye Wang, In Woodhead Publishing in Materials. Multifunctional Photocatalytic Materials for Energy, Woodhead Publishing 49–78
18. Liu Q (2020) Pollution and Treatment of Dye Waste-Water. IOP Conf Ser : Earth Environ Sci 514:052001
19. Liu Y, Yu YX, Zhang WD (2012) Photoelectrochemical properties of Ni-doped Fe_2O_3 thin films prepared by electrodeposition. Electrochim Acta 59:121–127

20. Mishra M, Chun DM (2015) α-Fe_2O_3 as a photocatalytic material: A review. Appl Catal A 498:126–141
21. Mohamed HH, Alomair NA, Akhtar S, Youssef TE (2019) Eco-friendly synthesized α-Fe_2O_3/TiO_2 heterojunction with enhanced visible light photocatalytic activity. J Photochem Photobiol A 382:111951
22. Ng YH, Lightcap IV, Goodwin K, Matsumura M, Kamat PV (2010) To What Extent Do Graphene Scaffolds Improve the Photovoltaic and Photocatalytic Response of TiO_2 Nanostructured Films? J Phys Chem Lett 1:2222–2227
23. Popov N, Ristić M, Bošković M, Perović M, Musić S, Stanković D, Krehula S (2022) Influence of Sn doping on the structural, magnetic, optical and photocatalytic properties of hematite (α-Fe_2O_3) nanoparticles. J Phys Chem Solids 161:110372
24. Rahman G, Joo OS (2013) Facile preparation of nanostructured α-Fe_2O_3 thin films with enhanced photoelectrochemical water splitting activity. Mater Chem Phys J Mater Chem A 1:5554–5561
25. Ren G, Han H, Wang Y, Liu S, Zhao J, Meng X, Li Z (2021) Recent Advances of Photocatalytic Application in Water Treatment: A Review. Nanomaterials 11:1804
26. Rostamizadeh E, Iranbakhsh A, Majd A et al (2020) Green synthesis of Fe_2O_3 nanoparticles using fruit extract of Cornus mas L. and its growth-promoting roles in Barley. J Nanostruct Chem 10:125–130
27. Samrot AV, Sahithya CS, Selvarani AJ, Purayil SK, Ponnaiah P (2021) A review on synthesis, characterization and potential biological applications of superparamagnetic iron oxide nanoparticles. Curr Res Green Sustainable Chem 4:100042
28. Shao W, Wang H, Zhang X (2018) Elemental doping for optimizing photocatalysis in semiconductors. Dalton Trans 47:12642–12646
29. Sharma S, Bhattacharya A (2017) Drinking water contamination and treatment techniques. Appl Water Sci 7:1043–1067
30. Suman CS, Kumar A, Kumar P (2020) Zn Doped α-Fe_2O_3: An Efficient Material for UV Driven Photocatalysis and Electrical Conductivity. Crystals 10:273
31. Syafrudin M, Kristanti RA, Yuniarto A, Hadibarata T, Rhee J, Al-onazi WA, Algarni TS, Almarri AH, Al-Mohaimeed AM (2021) Pesticides in Drinking Water—A Review. Int J Environ Res Public Health 18:468
32. Tadic M, Trpkov D, Kopanja L, Vojnovic S, Panjan M (2019) Hydrothermal synthesis of hematite (α-Fe_2O_3) nanoparticle forms: Synthesis conditions, structure, particle shape analysis, cytotoxicity and magnetic properties. J Alloys Compd 792:599–609
33. Thongam DD, Chaturvedi H (2021) Advances in nanomaterials for heterogeneous photocatalysis. Nano Ex 2:012005
34. Yilin, Liu et al (2017) Ultrafine Ti^{4+} doped α-Fe_2O_3 nanorod array photoanodes with high charge separation efficiency for solar water splitting. J Phys D: Appl Phys 50:255502

35. Yina Y, Zhang X, Sun C (2018) Transition-metal-doped Fe_2O_3 nanoparticles for oxygen evolution reaction. Progress in Natural Science: Materials International 28:430–436
36. Zielinska A, Kowalska E, Sobczak JW (2010) Synthesis, characterization and photocatalytic activity of magnetically separable γ-Fe_2O_3/N,Fe codoped TiO_2 heterojunction for degradation of reactive blue 4 dye. Sep Purif Technol 45:155–162

Figures

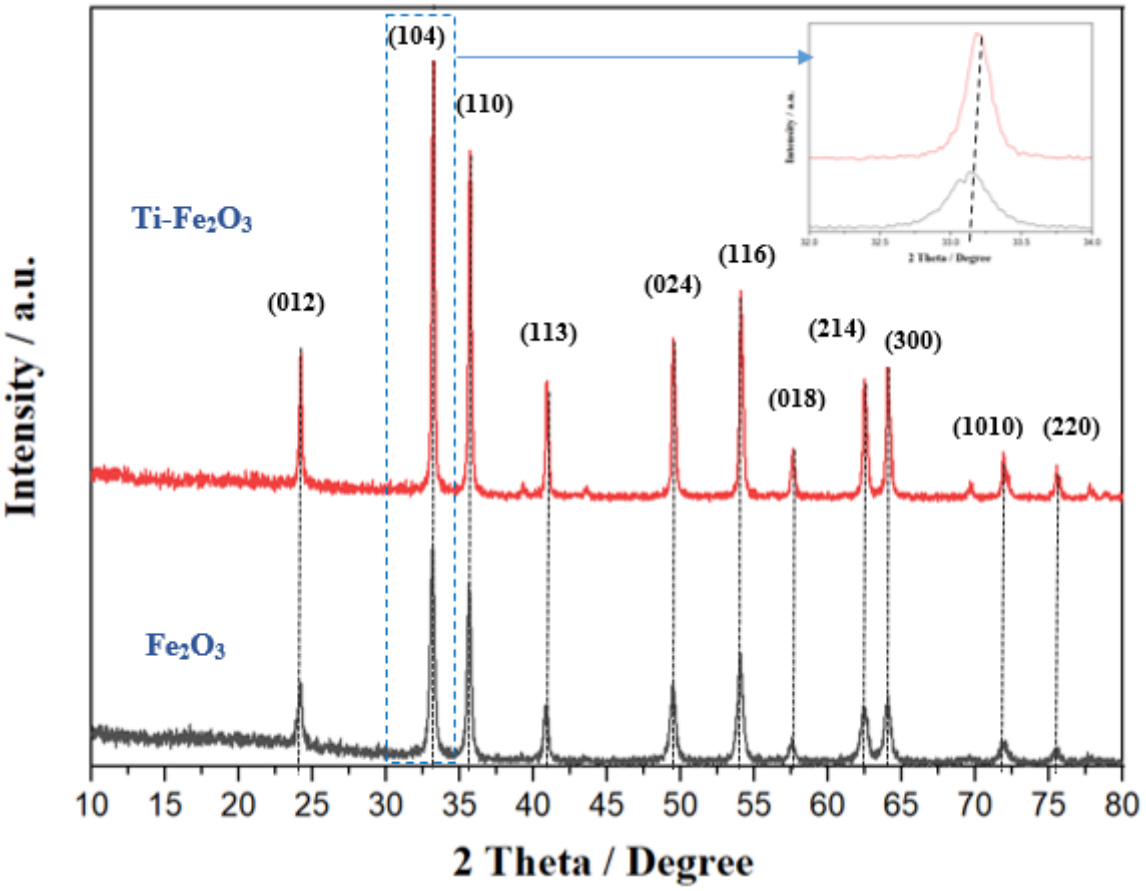

Figure 1

XRD patterns of Fe_2O_3 and Ti-Fe_2O_3 nanomaterials.

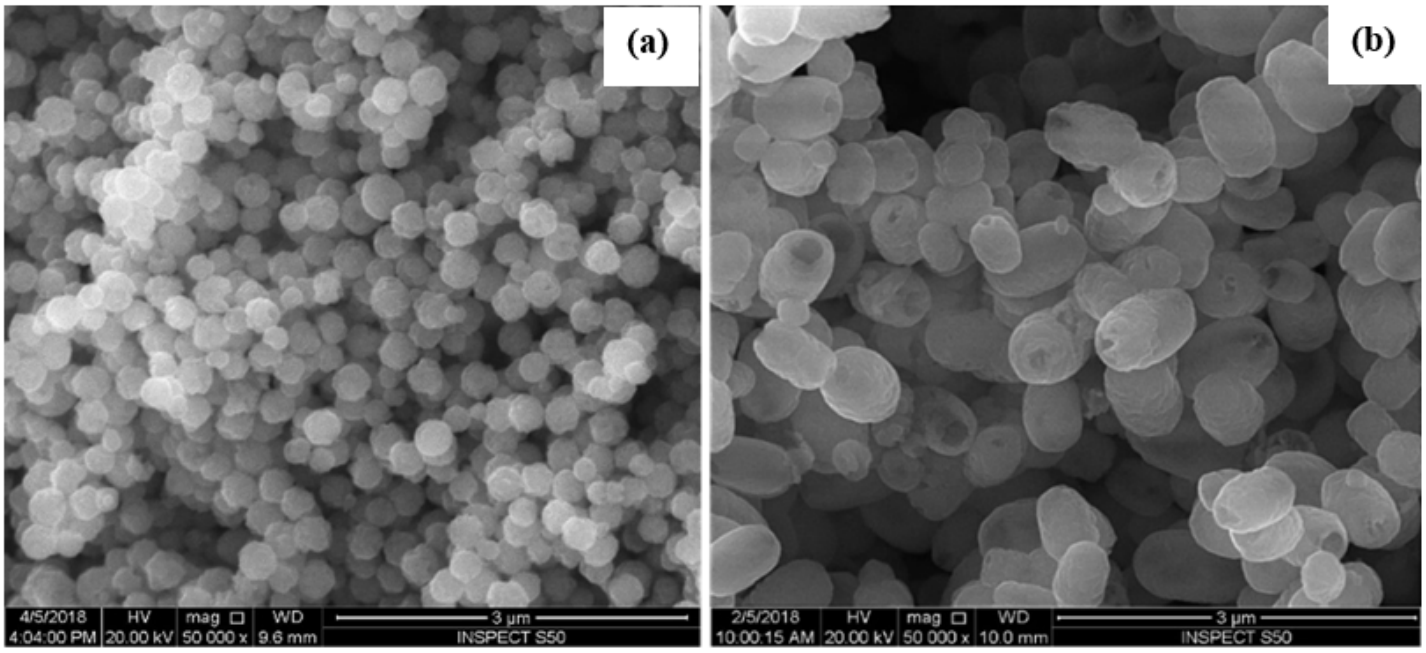

Figure 2

SEM images of Fe_2O_3 (a) and Ti-Fe_2O_3 (b) nanomaterials.

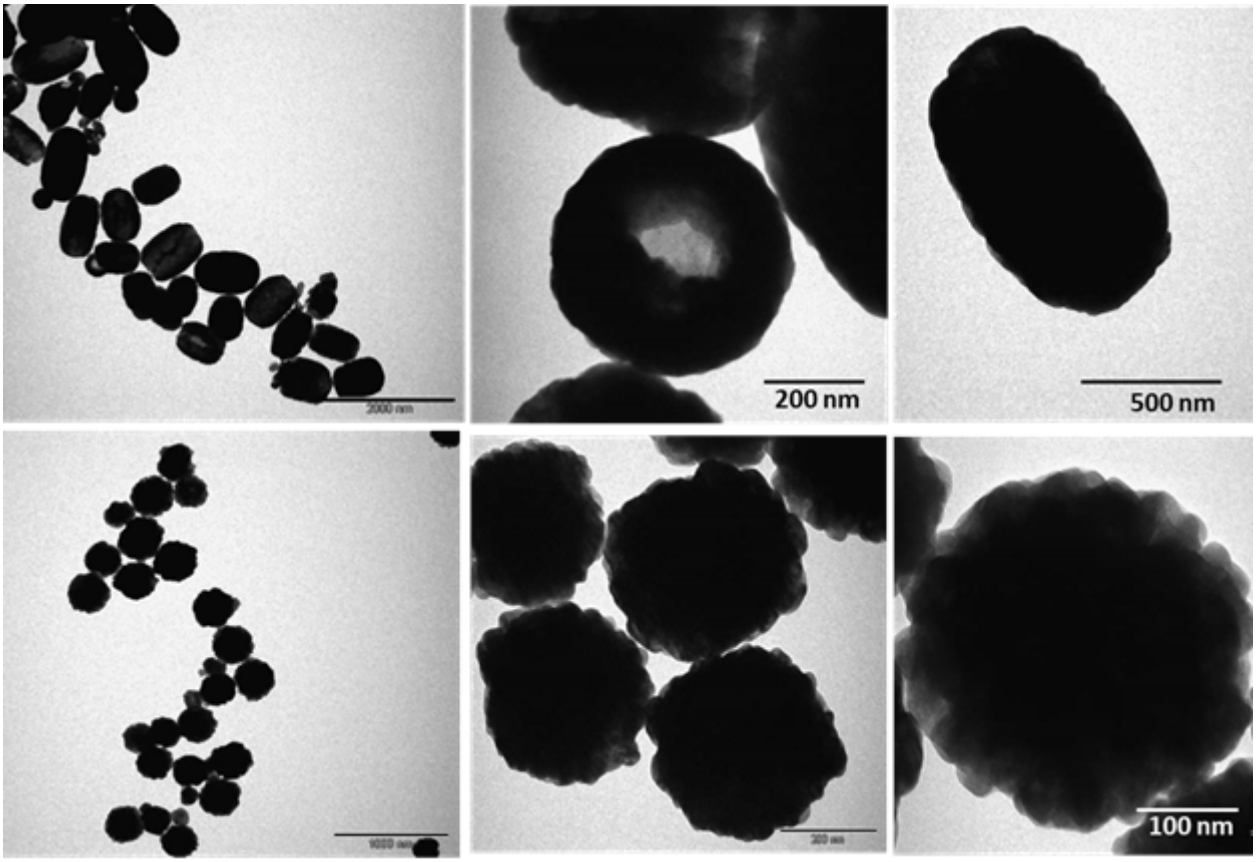

Figure 3

TEM images of Fe_2O_3 (a, b, c) and Ti-Fe_2O_3 (d, e, f) nanomaterials.

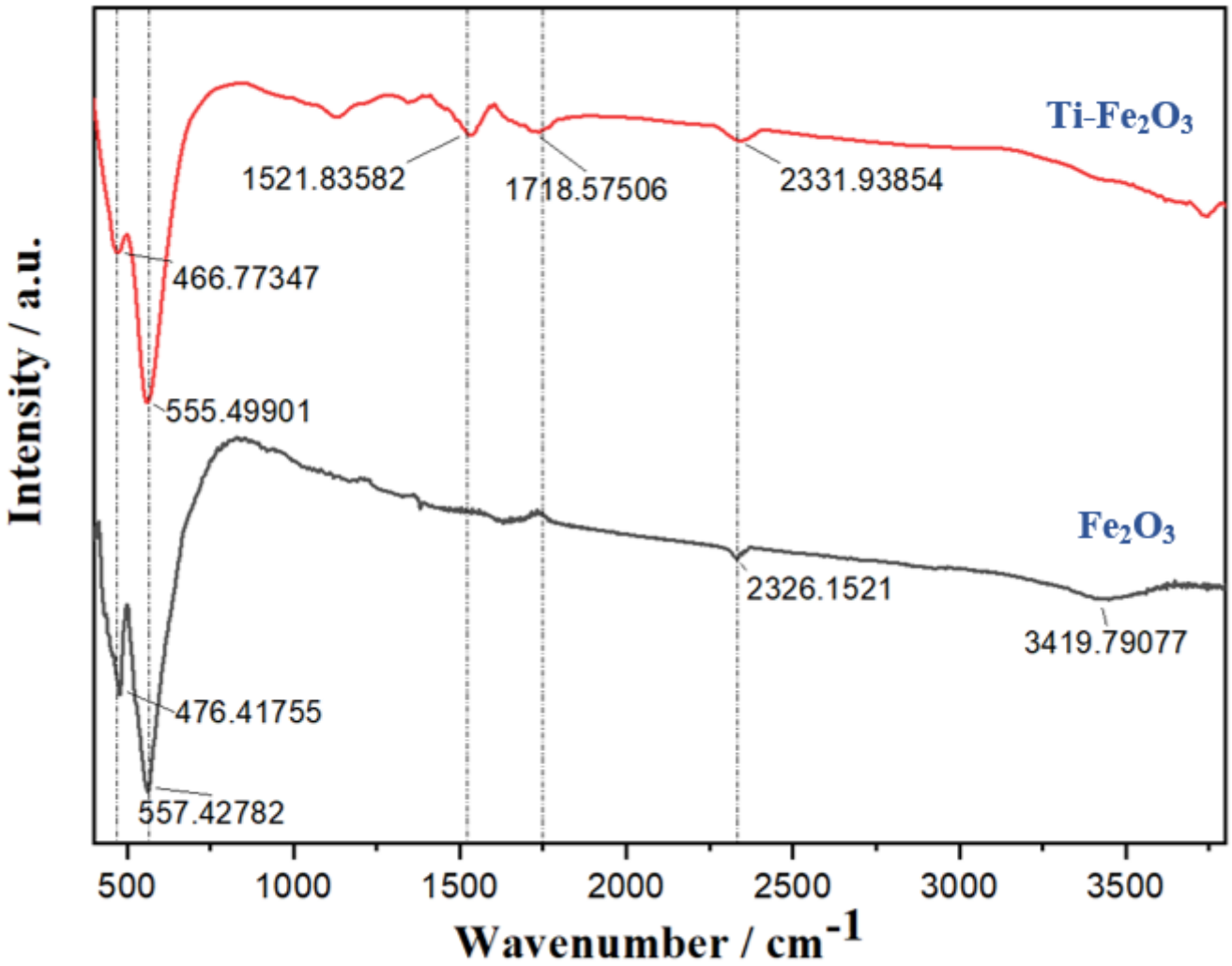

Figure 4

FTIR spectra of Fe2O3 and Ti-Fe2O3 nanomaterials.

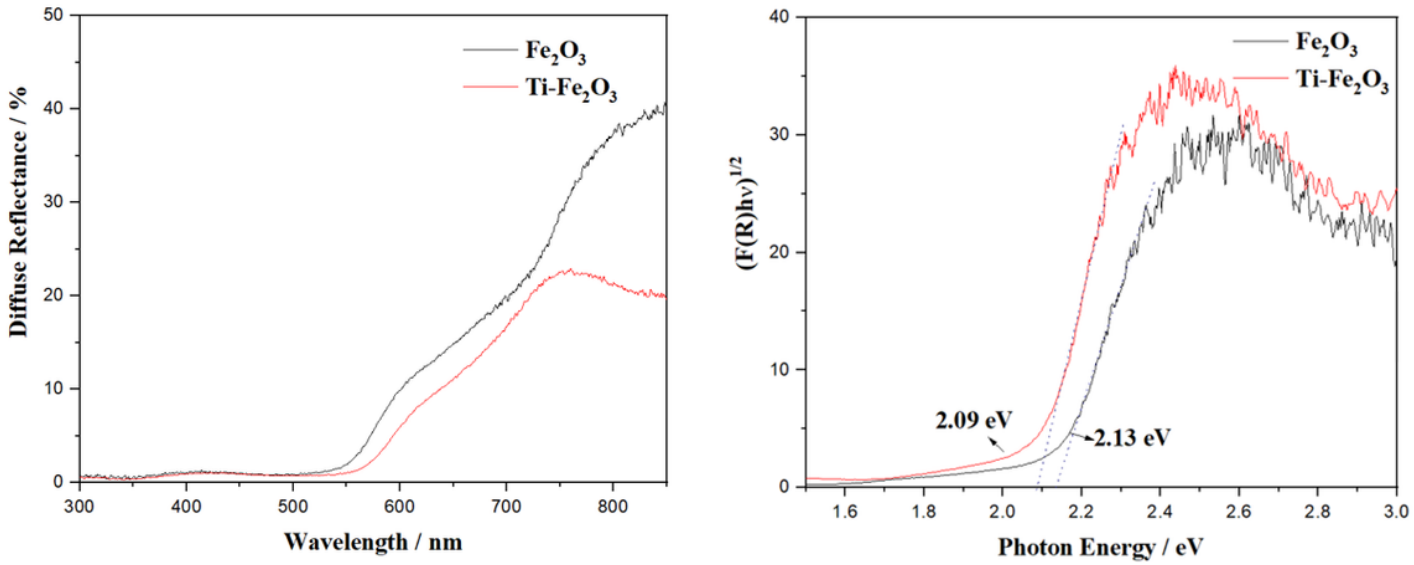

Figure 5

UV-vis Diffuse Reflectance (a) and Kubelka-Munk plot (b) of Fe_2O_3 and Ti-Fe_2O_3 nanomaterials.

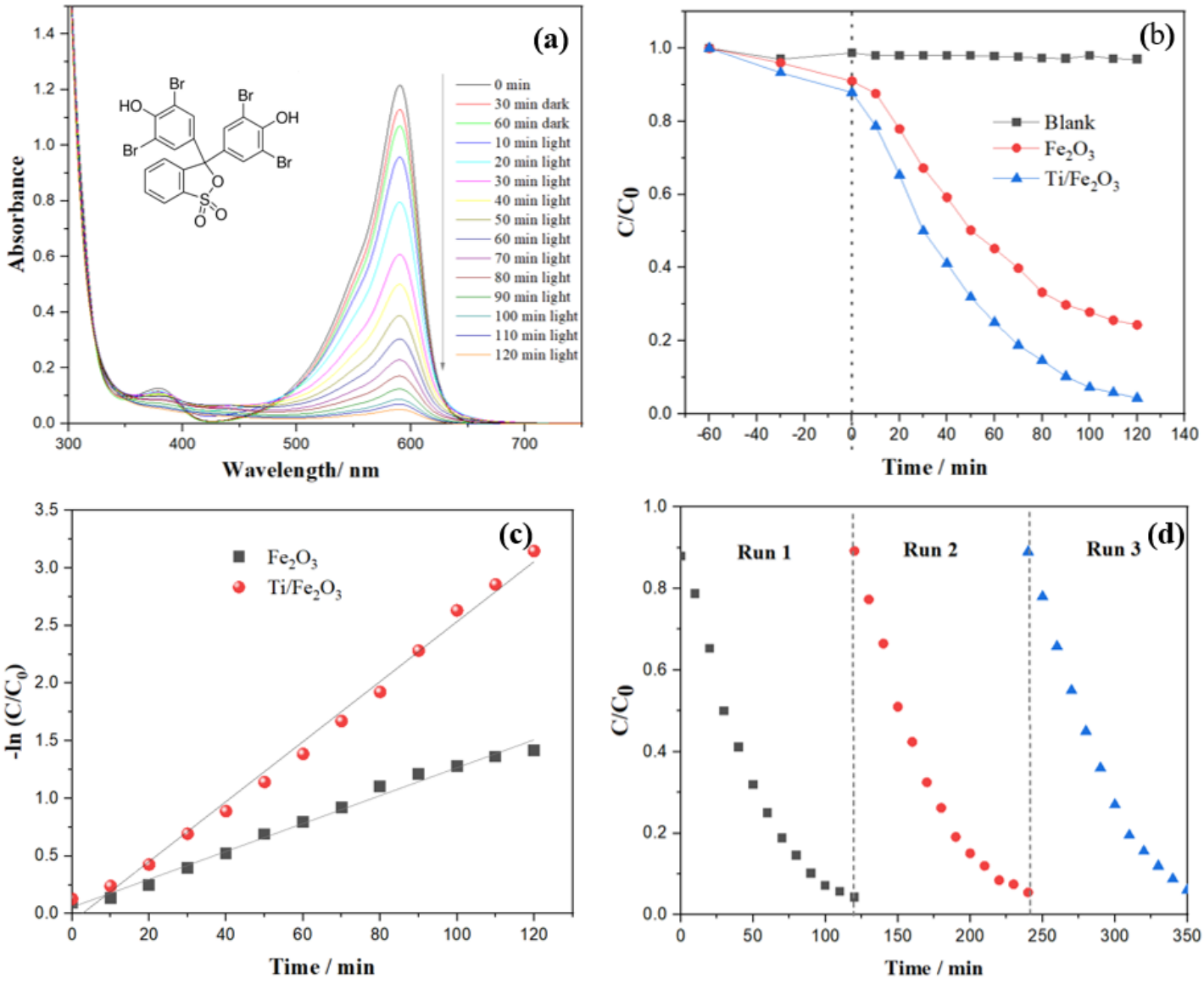

Figure 6

(a) UV–vis absorption spectra of an aqueous solution of BPB during solar light illumination using Ti-Fe_2O_3, (b) efficiency of the photocatalytic degradation of BPB as the variation of C/C_0 with irradiation time, (c) linear plots of – ln C/C_0 vs time for the experimental data in (b), (d) recyclability of Ti-Fe_2O_3.

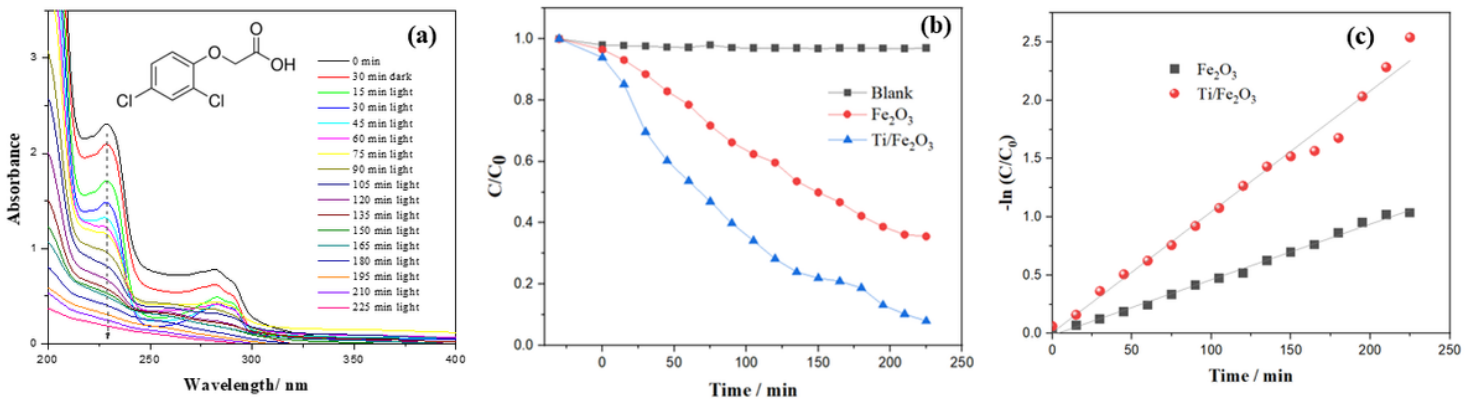

Figure 7

(a) UV–vis absorption spectra of an aqueous solution of 2,4-D during solar light illumination using Ti-Fe_2O_3, (b) efficiency of the photocatalytic degradation of 2,4-D as the variation of C/C_0 with irradiation time, (c) linear plots of $-\ln C/C_0$ vs time for the experimental data in (b).

Supplementary Files

This is a list of supplementary files associated with this preprint. Click to download.

- Suplementry.docx